remote sensing

MDPI

Article

First Galileo Single-Frequency Occultation Process and Precision Analysis of FengYun3E

Ming Yang [1,2,3,4], Xiangguang Meng [1,2,3,4,*], Haoran Tian [1,2,3,4], Yueqiang Sun [1,2,3,4], Qifei Du [1,2,3,4], Weihua Bai [1,2,3,4], Bowen Wang [1,2,3,4], Xianyi Wang [1,2,3,4], Peng Hu [1,2,3,4] and Guangyuan Tan [1,3,4]

1 National Space Science Center, Chinese Academy of Sciences, Beijing 100190, China; yangming212@mails.ucas.ac.cn (M.Y.)
2 School of Astronomy and Space Science, University of Chinese Academy of Sciences, Beijing 100049, China
3 Beijing Key Laboratory of Space Environment Exploration, Chinese Academy of Sciences, Beijing 100190, China
4 Key Laboratory of Science and Technology on Space Environment Situational Awareness, Chinese Academy of Sciences, Beijing 100190, China
* Correspondence: xgmeng@nssc.ac.cn

Abstract: This article proposes a single-frequency occultation method whose core is the reconstruction of a second frequency measurement. We process the actual received Galileo E1 single-frequency occultation observation data of FengYun3E to meet the urgent need for single-frequency Galileo occultation inversion of FengYun3 E/F/G/H satellites. Galileo single-frequency occultation events are globally distributed evenly and have stable quantities. The refractive index products and dry temperature products inverted from the single-frequency occultation data are reliable at altitudes of 5–30 km. The Galileo E1 single-frequency occultation process can effectively improve the output of FengYun3E/GNOS occultation products. These results validate the feasibility and correctness of using FengYun3/GNOS for the actual Galileo single-frequency occultation process. The atmospheric occultation products of Galileo single-frequency occultation increase the quantity of global occultation products and serve as a beneficial supplement to global numerical weather prediction data sources.

Keywords: FengYun3; Galileo occultation; single-frequency occultation process; reconstruction of a second frequency measurement

Citation: Yang, M.; Meng, X.; Tian, H.; Sun, Y.; Du, Q.; Bai, W.; Wang, B.; Wang, X.; Hu, P.; Tan, G. First Galileo Single-Frequency Occultation Process and Precision Analysis of FengYun3E. *Remote Sens.* **2023**, *15*, 4410. https://doi.org/10.3390/rs15184410

Academic Editor: Yuriy Kuleshov

Received: 16 August 2023
Revised: 4 September 2023
Accepted: 5 September 2023
Published: 7 September 2023

1. Introduction

Radio occultation (RO) technology was initially developed to explore the vertical profile parameters of the ionospheres and atmospheres of the planets in the solar system [1,2]. Subsequently, Fishbach proposed using a global navigation satellite system (GNSS) RO to probe the atmospheric parameters of the Earth [3]. The United States' Global Positioning System (GPS) became more mature in the late 1980s, and GNSS RO began to develop gradually and flourish. Currently, mature GNSS RO utilizes established GNSS systems such as BDS, GPS, Galileo, and GLONASS as signal transmitters, with GNSS receivers mounted on low-Earth-orbit satellites (LEOs) as observation platforms. By receiving and analyzing signal delay caused by the bending of the signal path, atmospheric parameters such as refractive index, pressure, temperature, humidity, and other related products can be retrieved through inversion, which are of great significance in improving numerical weather models, monitoring climate change, and studying atmospheric dynamic processes [4]. GNSS RO, with the capable of self-calibration and lack of bias, provides an effective complement to other data types, such as radiosondes and weather balloons [5]. Therefore, GNSS RO products from LEOs are one of the most significant factors in reducing errors in numerical weather prediction models [6]. If GNSS RO events are uniformly distributed globally, the greater the number of GNSS RO events is, the larger the volume of raw observational data available for inclusion in numerical weather prediction, leading to

higher prediction precision [5,7]. To increase the number of GNSS RO events and improve the precision of numerical weather prediction, some GNSS RO missions have employed the strategy of increasing the number of receiving GNSS RO signal systems. For example, the COSMIC-2 and SPIRE missions receive occultation signals from the GPS, Galileo, and GLONASS systems (https://data.cosmic.ucar.edu/gnss-ro/, accessed on 31 January 2022). The FengYun3 mission, starting from the FengYun3E (FY3E) satellite, receives occultation signals from the BDS, GPS, and Galileo systems.

China's second-generation polar-orbiting meteorological satellite mission, known as FengYun3, has been launched to address the challenges of three-dimensional atmospheric probes, greatly enhance global data collection capability, and further improve remote sensing capabilities for cloud and surface features [8]. The first FengYun3 satellite was launched in 2008 and six satellites have since been launched. As the fifth satellite, FY3E is the world's first civil Sun-synchronous polar-orbiting orbit meteorological satellite. It operates at an orbital height of 836 km and has an inclination angle of 98.75 degrees, allowing it to perform GNSS RO measurements covering the global range of the Earth [9]. FY3E was successfully launched on 5 July 2021, from the Jiuquan Satellite Launch Center in China using the Long March 4B carrier rocket. The remote sensing payload used for GNSS RO is called GNOS, which is unique in that it is the world's first payload capable of simultaneously performing GNSS RO measurements for the GPS, BDS 2&3, and Galileo systems [10]. Specifically, the FY3E occultation observation data are recorded in the ROEX format, which is an independent exchange format proposed by the National Space Science Center for easier GNSS RO data viewing and sharing. The ROEX format specifies the file type, composition structure, observed parameters, and data recording format of GNSS RO data. It is suitable for both independent exchange of space-based GNSS RO data and regional satellite navigation system GNSS RO data [11].

Initially, the GNOS onboard FY3C and FY3D satellites received dual-frequency GPS and BDS-2 occultation signals. Subsequently, FY3E, FY3F, FY3G, and FY3H are capable of simultaneously receiving GNSS RO signals from GPS, BDS-2&3, and Galileo systems. It should be noted that, due to resource constraints, the reception was limited to dual-frequency RO signals from GPS and BDS systems, along with single-frequency RO signals from the Galileo system. Due to the difficulty in mitigating ionospheric effects with only single-frequency measurements, the conventional dual-frequency occultation process is not suitable for the Galileo single-frequency occultation process. Therefore, there is an urgent need to develop Galileo single-frequency occultation inversion algorithms. In previous experiments, researchers tested the GPS RO signals received by the Turborogue receiver on the Ørsted launched in February 1999. The results showed that compared to the dual-frequency occultation process, the accuracy of the single-frequency atmospheric occultation process was more affected by ionospheric effects and lower in precision above an altitude of 30 hPa. Montenbruck et al. used GPS L1 single-frequency amplitude and carrier phase observations for occultation inversion, which yielded slightly lower precision in refractive index products compared to dual-frequency occultation inversion [12]. Larsen et al. reconstructed the second frequency using GPS L1 single-frequency pseudorange and carrier phase observations for a single-frequency occultation process on Ørsted. The refractive index products and dry temperature products showed relatively good precision compared to the European Centre for Medium-Range Weather Forecasts (ECMWFs) [13]. However, Larsen et al. utilized the double differencing method for single-frequency occultation product inversion. While this approach reduces observation errors, it amplifies observation noise. Additionally, using a single differencing method or a zero-difference method for the GNSS RO process are both viable options. The single differencing method eliminates the receiver clock bias through differencing between the occultation-LEO link and the reference-LEO link. Since measurements from the reference satellite are single-frequency, eliminating ionospheric effects using the reference-LEO link will introduce pseudorange measurement noise. In the case of the zero-difference method, if the stability

of the GNOS clock bias is high, it can improve the inversion precision of the zero-difference method and achieve similar inversion precision as the single differencing method [14].

During the algorithm verification stage, we have already processed GPS single-frequency occultation data and BDS single-frequency occultation data from FY3E/GNOS, utilizing the single-frequency occultation process of reconstructing the second frequency with the zero-difference method. We have compared the processed products with the products derived from the dual-frequency occultation process and ERA5 reanalysis to assess their precision [15,16]. Compared with the dual-frequency occultation inversion, the correlation coefficient of the relative total electron content (relTEC) for single-frequency GPS and single-frequency BDS occultation inversion is greater than 0.95. The average deviation of the excess phase Doppler for single-frequency inversion is mostly less than 0.2%. The refractive index product obtained from single-frequency inversion has slightly lower precision compared to the dual-frequency inversion product, but they show good consistency in terms of deviation and root mean square (RMS) indicators compared to ERA5 reanalysis. This verifies the feasibility of the proposed method. In this study, actual FY3E Galileo single-frequency occultation observations were used for product inversion and precision analysis, with the aim of providing more occultation data for numerical weather prediction.

Section 2 of this paper describes the FY3E/GNOS Galileo E1 single-frequency occultation process method. In Section 3, the global distribution of occultation events during the operational period of FY3E/GNOS is analyzed. Subsequent Sections 3.2 and 3.3 evaluate the precision of the refractive index product and the dry temperature product inverted from the Galileo single-frequency occultation process. Section 4 summarizes the research findings, and Section 5 discusses the potential applications of the single-frequency occultation process.

2. Galileo E1 Single-Frequency Occultation Process Method

Figure 1 shows the Galileo E1 single-frequency occultation process flow, which includes the following steps:

1. FY3E/GNOS Level 0 data are segmented, converted into an appropriate format, and preprocessed to positioning observation data and occultation observation data.
2. FY3E precise orbit determination (POD) using FY3E positioning observation data and accurate GNSS products from IGS, resulting in precise position, velocity, and receiver clock bias.
3. Reconstruction of the carrier phase occultation observation data at the second frequency using pseudorange and carrier phase occultation observation data at Galileo E1 single-frequency.
4. Computation of the neutral atmosphere excess phase using the results from the previous three steps.
5. Inversion of the neutral atmosphere bending angle and refractive index using Abel integral transformation.
6. Retrieval of atmospheric temperature based on refractive index.

FY3E/GNOS includes two sets of positioning antennas, each with a corresponding RF unit, as well as two sets of atmospheric occultation antennas, each also equipped with an RF unit, in addition to a data processing unit. The antennas utilize low noise RF front end technology to ensure effective capture and processing of GNSS signals. The central frequencies of the receiver channels are shown in Table 1. FY3E/GNOS simultaneously receives positioning signals and occultation signals: GPS L1&L2, BDS B1&B3, and Galileo E1 [17]. The GNSS RO data record rule in GNOS is that when a rise or set GNSS RO event occurs, the carrier phase and amplitude of the radio signals are recorded at a high sampling rate of 50 Hz. The sampling rate in the pseudorange is recorded at a range of 1–50 Hz [18].

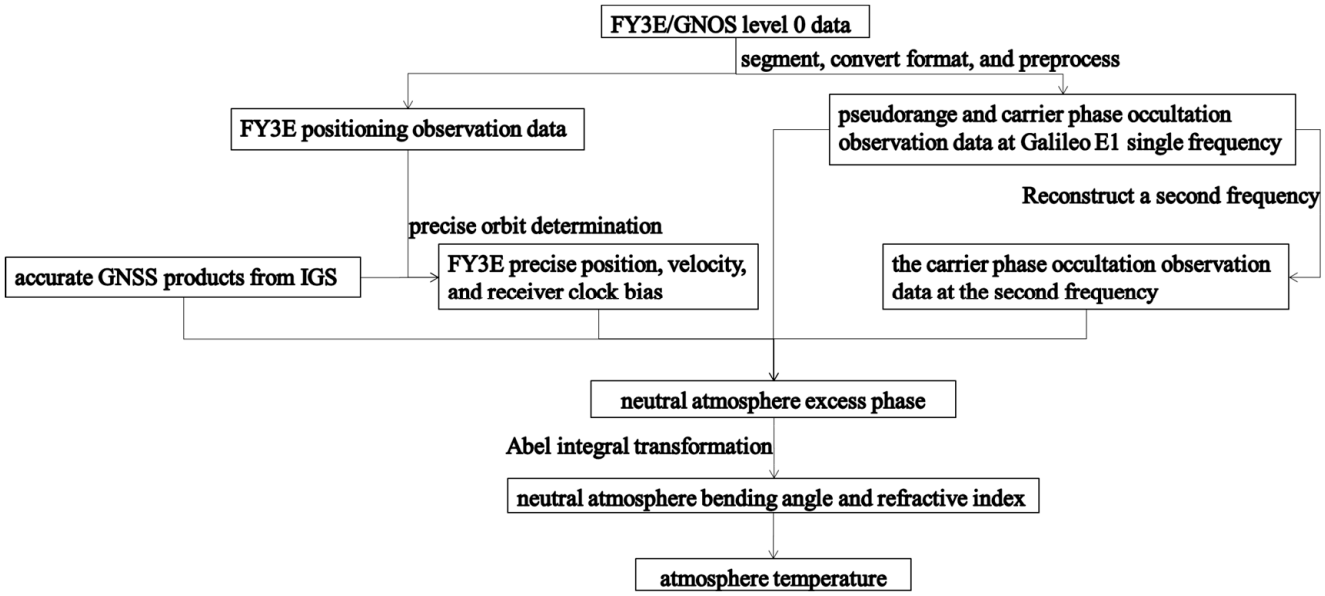

Figure 1. FY3E/GNOS Galileo E1 single-frequency occultation process flow.

Table 1. Center Frequencies of GNSS Navigation Signal Channels for FY3E Occultation Detection.

System	Band	Frequency (MHz)
GPS	L1	1575.42
	L2	1227.60
BDS	B1	1561.098
	B3	1268.52
Galileo	E1	1575.42

Because Galileo positioning data have a single-frequency and Galileo positioning channels are significantly fewer than those of GPS, we utilize GPS L1&L2 positioning observation data for ground POD. The satellite position and velocity coordinates are all within the framework of the Earth-centered inertial coordinate system in the FY3E POD. FY3E is equipped with two positioning antennas, and the simplified dynamics method is employed by merging the observation data from the half field of view of the two antennas [19]. The POD is computed at intervals of 30 s, and all GPS positioning observation data are processed in batches with a duration of 30 h. The fundamental observations used are ionosphere-free pseudorange and phase combinations. State vectors, including position, velocity, and clock bias, are estimated, along with empirical segment constants for acceleration (with 90 min intervals) and atmospheric drag (with 6-h intervals). The estimated results from each iteration are used as the initial orbit for the next iteration until the estimation residuals are sufficiently small.

In the radial-tangential-normal (RTN) reference coordinate system, POD achieves precision in position and velocity, using the RMS errors from overlapping arc segments as indicators. Figure 2 illustrates the RMS errors for a 14-day FY3E POD analysis. Subfigure (A) represents the positional precision, which is lower than 2.5 cm along the T direction, and the average 3D RMS position precision is 1.91 cm. Subfigure (B) represents the velocity precision, which is lower than 25 μm/s along the R direction and, the average 3D RMS velocity precision is 15.96 μm/s. The computed position and velocity precision are sufficient for the inversion of atmospheric occultation products.

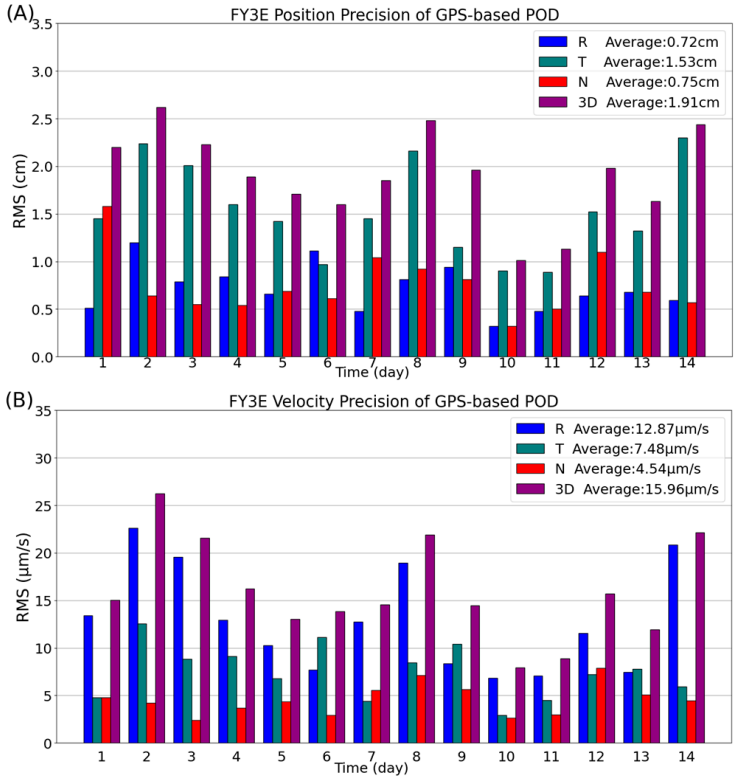

Figure 2. Fourteen-day RMS errors of FY3E POD based on GPS positioning observation data. Subfigure (**A**): the position precision; subfigure (**B**): the velocity precision.

2.1. Reconstruct a Second Frequency Measurement

The previous section provided an overview of the characteristics of GNOS Galileo E1 occultation observation data and the FY3E POD. This section will discuss the reconstruction of the second frequency for the Galileo E1 single-frequency occultation process. Specifically, the reconstruction of the carrier phase measurement of the second frequency is based on the Galileo E1 single-frequency pseudorange measurement E_1 and carrier phase measurement C_1. In theory, the choice of the second frequency is arbitrary, but for the versatility of the occultation Level 2 product process, the second frequency in this paper is based on the E5a in Galileo's dual-frequency measurement, with a frequency of 1176.45 MHz.

The reconstructed occultation carrier phase measurement E_{5a}^{*} is greatly affected by occultation pseudorange measurement noise. Therefore, a regularization method that minimizes the second derivative is commonly used to filter the noise in the occultation pseudorange measurements to reduce its impact on E_{5a}^{*} [20–22]. The first step is to construct a filtering matrix F. This is done by interpolating and patching the data gaps in E_1 (sampled at a rate of 50 Hz) and C_1 (sampled at a rate of 1–50 Hz) using a regularization parameter γ, thereby reducing the noise influence from the observations. A value of γ equal to 10^6 is chosen for a smoothing strength that corresponds to a low-pass filter with a cutoff frequency of approximately 0.05 Hz. To unify the sampling rates of E_1 and C_1 to 50 Hz, the size of the filtering matrix should be 500 × 500. Equation (1) represents the calculation formula for the filtering matrix F in the regularization method that minimizes the second derivative [13]:

$$\mathrm{F} = \left(\widetilde{\mathrm{I}} + \gamma \mathrm{S}^{\mathrm{T}}\mathrm{S}\right)^{-1} \quad (1)$$

where $\widetilde{\mathrm{I}}$ is a diagonal matrix, in which the corresponding diagonal elements are set to 1 at the positions where data exist in both E_1 and C_1, and the remaining elements are set to 0. Its size is 500 × 500. The matrix S is a finite difference operator for the second derivative, which is represented by S^T as its transpose.

The second step is to calculate the reconstructed carrier phase measurements, denoted as E^*_{5a} [13].

$$E^*_{5a} = E_1 - 0.5\left(1 - \frac{{f_1}^2}{{f_2}^2}\right)F(E_1 - C_1) \quad (2)$$

As shown in Equation (2), the E5a frequency carrier phase measurement E^*_{5a} is calculated by subtracting the carrier phase measurement E_1 from the filtered $E_1 - C_1$. Here, f_1 represents the frequency of the Galileo E1 signal, and f_2 represents the frequency of the Galileo E5a signal, both measured in Hz. Then, the term $E^*_{5a} - C_1$ can be used to invert the reconstructed relTEC of the second frequency, measured in total electron content units (TECUs). It has been statistically observed that the range of relTEC falls within 20 TECUs. The relTEC variation rate is involved in the excess phase Doppler calculation [23]. Therefore, Figure 3 illustrates the reconstructed relTEC variation rate for two representative occultation events, as shown in subplots (A) and (B). In particular, the calculation of the rate has nothing to do with the type of occultation rising or setting, and is based on the tangent point height from low to high. As can be seen from the figure, the relTEC variation rate is always positive, which indicates that relTEC is always increasing within 120 km.

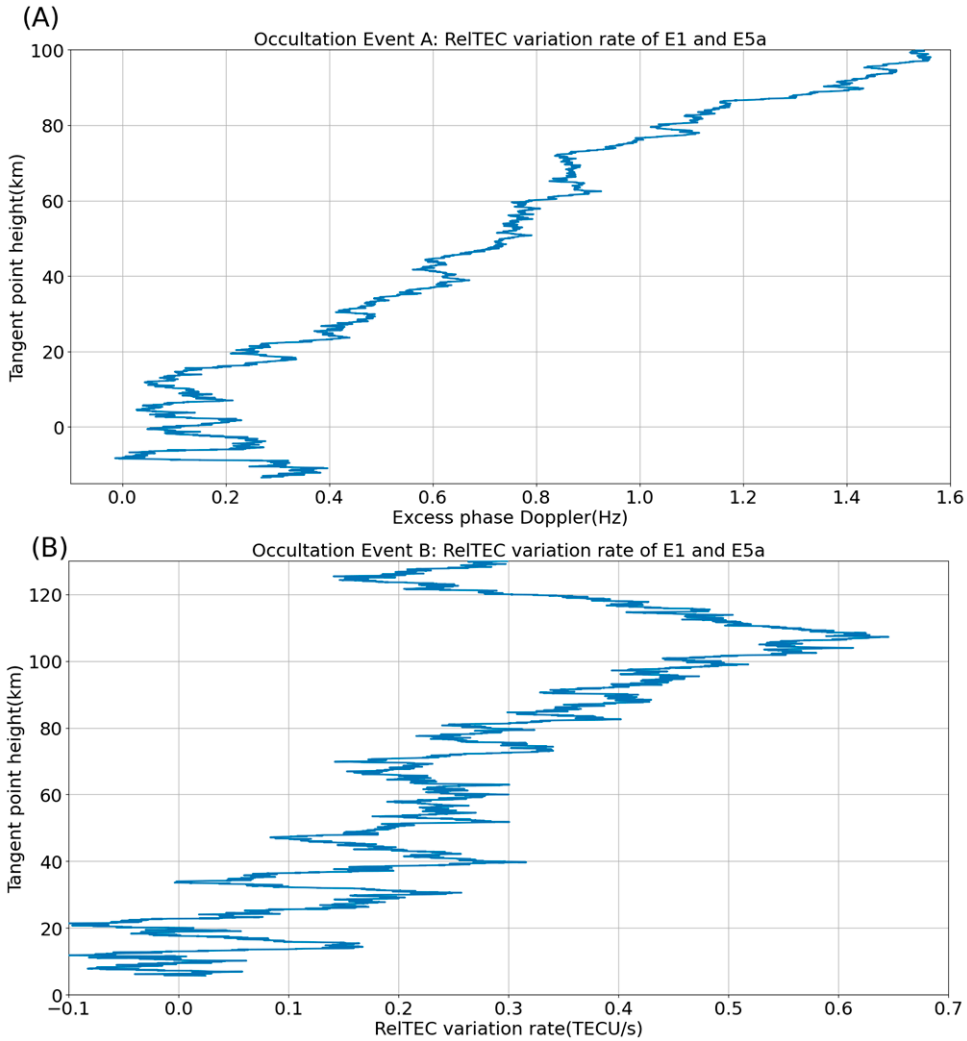

Figure 3. The relTEC variation rate at the reconstructed second frequency, with subplots (**A**,**B**) depicting two representative occultation events.

2.2. Excess Phase Calculation

The initial purpose of reconstructing the second frequency is to adapt the Galileo E1 single-frequency occultation inversion algorithm to general GNSS occultation Level 2 inversion software (ROPP 6.0 is used in this paper). Figure 4 shows an illustration of a GNSS RO. FY3E (denoted by A) simultaneously receives signals from the GNSS satellite (denoted by B) undergoing an occultation event and signals from a high elevation angle GNSS satellite (denoted by C). The red path represents the bending of the signal in the atmosphere. In this case, AB represents the occultation-LEO link, and AC represents the reference-LEO link. In the single difference method, the AB observation equation is subtracted from the AC observation equation to eliminate the receiver clock bias. However, since the reference satellite C measurement is also a single frequency, the solution is affected by the noise in the reference satellite pseudorange measurement. Fortunately, the FY3E/GNOS clock has stability reaching the order of 10^{-12} in one second, and the clock drift precision is sufficient for calculating the excess phase with relatively high precision using the zero-difference method.

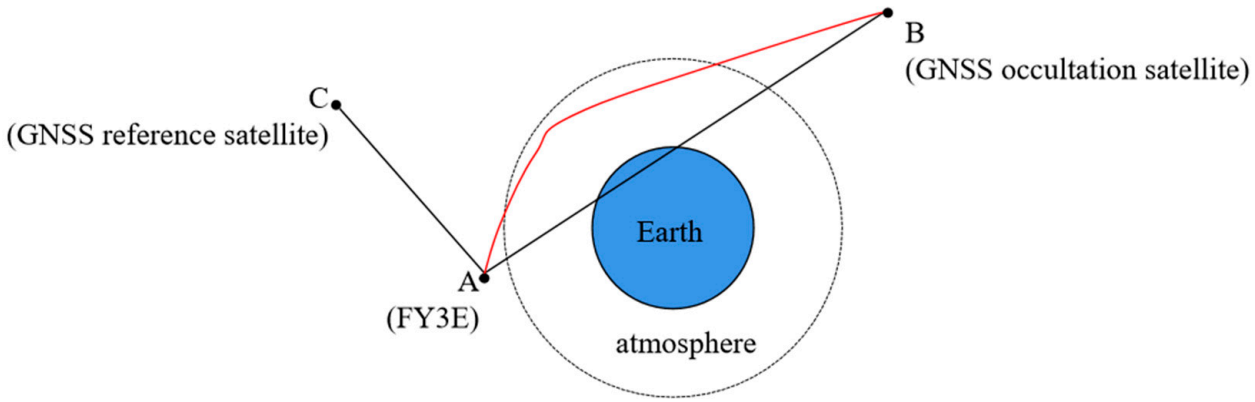

Figure 4. Schematic of GNSS RO. The red line refers to the actual propagation route of the RO signal.

The calculation of the excess phase using the zero-difference method only involves link AB and does not include link AC. This is expressed in Equation (3):

$$\begin{aligned}\delta_{ex,i}(t_r) = {} & r_A^B(t_r) - E_i(t_r) + c\cdot(\delta_A(t_r) - \delta_{A,rel}(t_r)) \\ -c\cdot\left(\delta^B(t_r - \tau_A^B) - \delta_{rel}^B(t_r - \tau_A^B)\right) & + \delta\rho_{A,rel}^B(t_r) + \Delta\varphi_A^B(t_r) + \varepsilon\end{aligned} \quad (3)$$

In the equation, t_r represents the time of GNOS signal reception. i represents the frequency of either E_1 or E_{5a}^*. $\delta_{ex,i}$, r_A^B, E_i, and $\Delta\varphi_A^B(t_r)$ represent the excess phase, geometric distance AB, carrier phase observation of E1 or reconstructed carrier phase observation of E5a, and corresponding phase ambiguity correction, respectively. Their units are all meters. c is the speed of light, taken as a constant value of 2.99792458×10^8 m/s. For the time-related parameters, δ_A and δ^B represent the clock biases of satellites A and B, respectively; $\delta_{A,rel}$ and δ_{rel}^B represent the relativistic effects on the clock biases of satellites A and B, respectively; and τ_A^B represents the radio wave propagation time. $\delta\rho_{A,rel}^B$ represents the relativistic effects, excluding clock biases. All time-related parameters are expressed in units of seconds. Information regarding the positions, velocities, and clock biases is obtained through POD. Additionally, ε represents measurement noise.

The excess phase Doppler is the input for refractive index product inversion. Therefore, it is necessary to convert the excess phase into excess phase Doppler [24]. The equation for calculating the excess phase Doppler corresponding to the E1 and E5a frequencies is as follows:

$$\Delta D_i = -\frac{1}{\lambda_i}\cdot\frac{d\delta_{ex,i}}{dt} \quad (4)$$

The equation above, where λ_i represents the wavelength of frequency i, provides the excess phase Doppler calculated from the E1 frequency occultation data and the reconstructed excess phase Doppler calculated from the E5a frequency observation data. Figure 5A,B illustrate two representative occultation events. The x-axis represents the excess phase Doppler in Hz, while the y-axis represents the height in km in the form of a logarithmic axis.

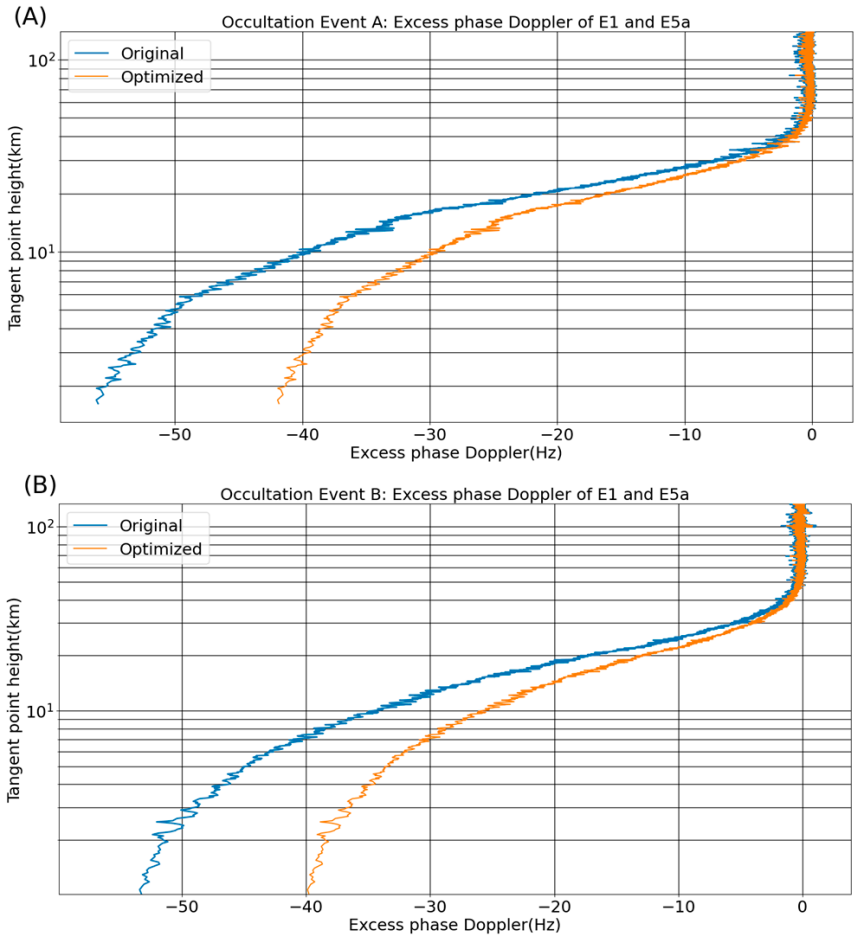

Figure 5. Excess phase Doppler corresponding to heights ranging from 0 to 140 km. Subfigures (**A**,**B**) represent two representative occultation events. The excess phase Doppler calculated from the E1 frequency occultation data is represented by the blue curve, while the excess phase Doppler calculated from the reconstructed E5a observation data is represented by the orange curve.

From the figures, during the initial stages of occultation, the excess phase Doppler is close to zero. As the height decreases, the excess Doppler delay undergoes significant changes. This is because when the ray's tangent point crosses the ionosphere and upper troposphere, where the medium is relatively thin, the signal amplitude remains relatively constant, resulting in the excess phase Doppler being close to zero. However, as the ray descends through the atmosphere, the refractive index becomes stronger, causing the ray to bend more, thus leading to a noticeable change in the excess Doppler delay [25].

2.3. Inversion of Refractive Index Product and Temperature Product

Figure 6 illustrates the geometric optical model of GNSS RO. Assuming atmospheric symmetry, the rays in the figure are restricted to the same plane. l_A and l_B represent unit vectors in the direction of signal transmission for satellites A and B, respectively. α indicates the bending angle of the occultation event. r and v denote the position and velocity of the satellite obtained from POD.

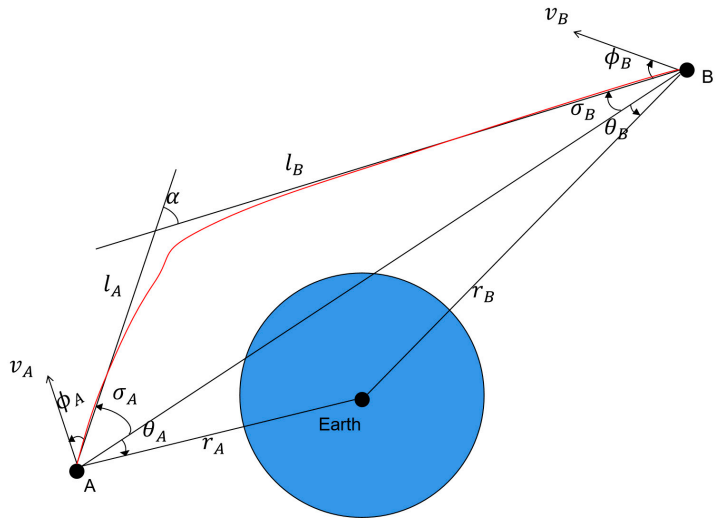

Figure 6. The geometric optical model of GNSS RO. The meaning of the line segment is the same as in Figure 4, l represents the tangent of the actual route, and v represents the satellite's velocity vector.

With the aid of the quantities illustrated in Figure 6, the excess phase Doppler can be expressed as:

$$\lambda_i \cdot \Delta D_i = v_B \cos(\phi_{B,i} - \delta_{B,i}) - v_A \cos(\phi_{A,i} - \delta_{A,i}) - (v_A \cos(\phi_{A,i}) - v_B \cos(\phi_{B,i})) \quad (5)$$

Thus, the above equation has only two unknowns, δ_A and δ_B. Using Snell's law in a spherically symmetric medium, we have the following equation:

$$n(r_A) \sin(\phi_{A,i} + \delta_{A,i}) = n(r_B) \sin(\phi_{B,i} + \delta_{B,i}) \quad (6)$$

$n(r_A)$ and $n(r_B)$ represent the refractive indices at the positions of the FY3E and GNSS satellites, respectively, and can be approximated as 1. Utilizing Equations (5) and (6), the bending angle α_i can be calculated as follows:

$$\alpha_i = \delta_{A,i} + \delta_{B,i} \quad (7)$$

Eliminating the ionospheric influence is crucial in inverting atmospheric products. Due to the dispersive effects of the ionosphere, the bending angle profiles calculated using Galileo E1 and reconstructed E5a exhibit differences. It can be assumed that the first-order term of the ionospheric bending angle can be eliminated through a linear combination using Equation (8) and a represents the impact parameter:

$$\alpha(a) = \frac{f_1^2 \alpha_{E1}(a) - f_2^2 \alpha_{E5a}(a)}{f_1^2 - f_2^2} \quad (8)$$

In the upper atmosphere above 40 km, the bending angle is relatively small, and the received signal is lower than the receiver's thermal noise level. Therefore, it is necessary to employ a statistical optimization method to further eliminate ionospheric errors [26]. Figure 7 shows the bending angle profiles originally and optimized by statistical optimization method, which can effectively correct the scene of sharp changes in the bending angle of the original data. This is because that the statistical optimization method combines measurement and bending angle of models. The coefficients are statistically optimized based on the noise characteristics of the bending angles, extrapolating from reliable low-altitude data to unreliable high-altitude data. Additionally, it incorporates bending angle intervention obtained from the a priori climatological model in mass spectrometer and incoherent scatter (MSIS) data [27,28].

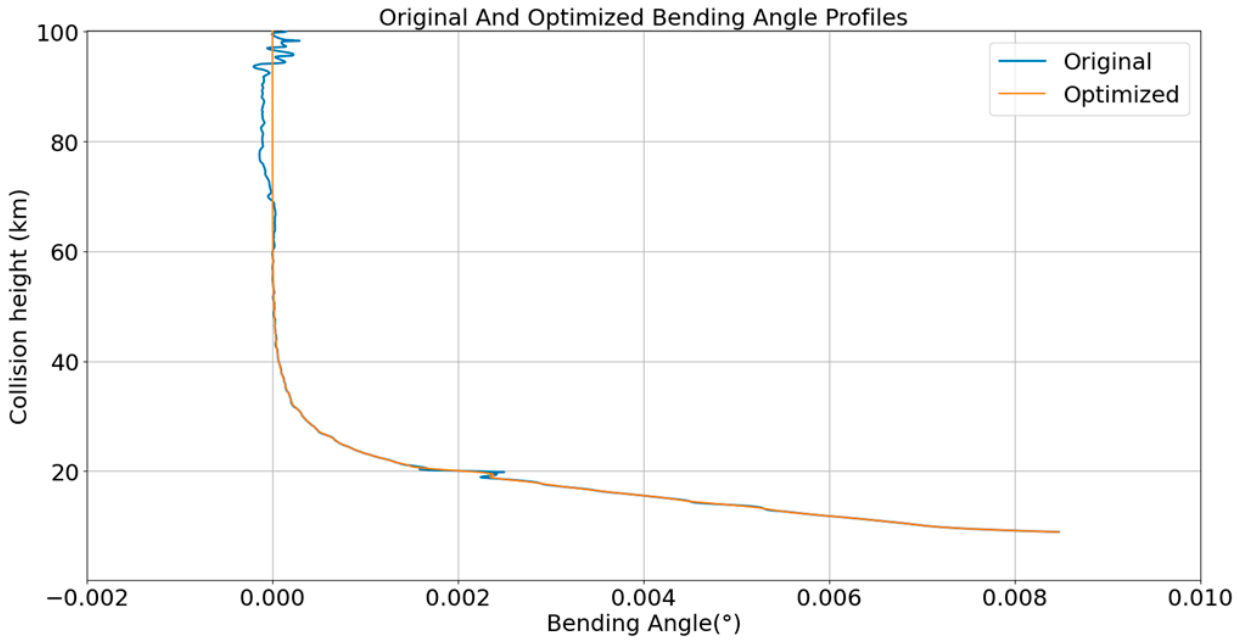

Figure 7. Original and optimized bending angle profiles.

Under atmospheric symmetry, the atmospheric refractive index can be obtained through the Abel integral transform using Equation (9):

$$N(a_0) = \exp\left(\frac{1}{\pi}\int_{a_0}^{\infty}\frac{\alpha(a)}{\sqrt{a^2 - a_0^2}}da\right) \tag{9}$$

In the equation, the additional parameters represent the following: N represents the atmospheric refractive index, a_0 corresponds to the impact parameter specific to the current occultation. Both the bending angle and refractive index can be directly assimilated into numerical weather prediction models. With the assistance of numerical weather prediction models as prior information on the atmospheric state, the refractive index can be further inverted into meteorological parameters such as temperature using Equation (10):

$$N = 77.6\frac{P}{T} + 3.73 \cdot 10^5\frac{P_W}{T^2} \tag{10}$$

In the equation, P represents atmospheric pressure in units of hPa, T represents the absolute temperature of the atmosphere in Kelvin (K), and P_W represents water vapor pressure. The first term on the right side represents the contribution of dry air to the refractive index, while the second term represents the contribution of water vapor. By neglecting the influence of moisture in the atmosphere, we can obtain the dry temperature:

$$T = 77.6\frac{P}{N} \tag{11}$$

When inverting for single-frequency occultation products, the largest error comes from the delay caused by the radio signal passing through the ionosphere. In this paper, a reconstruction of the second frequency is performed to calculate the excess phase, which is then used to validate the data through excess phase Doppler. In the bending angle calculation, the error associated with the first-order term of the ionosphere is eliminated, and the upper atmospheric ionospheric error is mitigated with the assistance of climatological models. This approach enables the inversion of occultation products with higher precision.

3. Results

3.1. Distribution and Number of Galileo E1 Single-Frequency Occultation Events

As mentioned above, if the occultation events are more evenly distributed globally, the consistency of the precision of global numerical weather prediction will be improved in terms of geographical distribution. Figure 8A–C illustrate the global distribution of atmospheric occultation events received by FY3E/GNOS for Galileo, GPS, and BDS on 1 January 2022. The red upright triangles represent rising occultation events, while the blue inverted triangles represent setting occultation events. From the figures, the number of rising and setting occultation events is comparable for a day. Similar to GPS and BDS, Galileo occultation events are uniformly distributed worldwide.

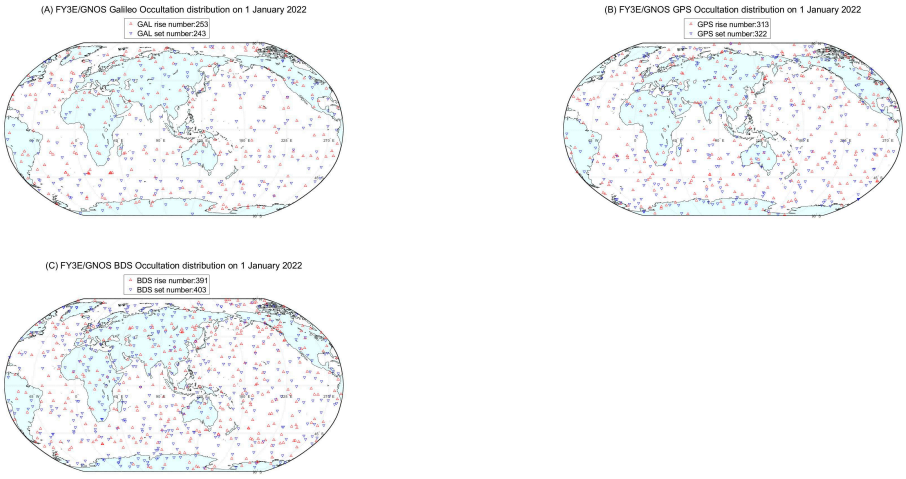

Figure 8. Distribution of atmospheric occultation events on 1 January 2022, with occultation signals coming from Galileo (**A**), GPS (**B**) and BDS (**C**).

If the Galileo single-frequency occultation process is successful, it will significantly increase the number of FY3E occultation inversion products. Figure 9 shows statistics of FY3E/GNOS occultation events received from 1 January to 14 January 2022. On average, FY3E/GNOS received 480 Galileo occultation events per day, 790 BDS occultation events, and 630 GPS occultation events. Conducting occultation events with all three systems increased the number by 33.8% compared to observations with BDS and GPS. As shown in the figure, the continuous 14-day occultation reception quantity remains relatively stable, indicating that the instrument could consistently receive occultation events from various navigation satellite systems.

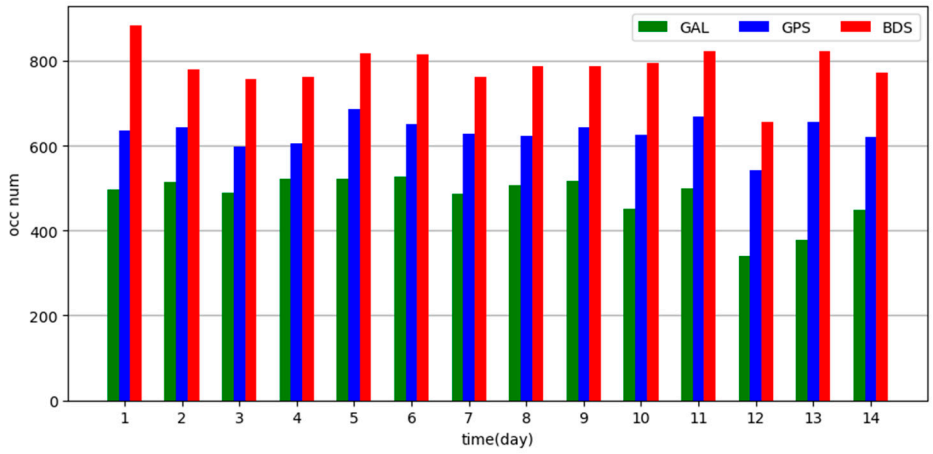

Figure 9. Number of atmospheric occultation events from 1 to 14 January 2022, with occultation signals coming from Galileo, GPS and BDS, respectively.

3.2. Precision Analysis of the Refractive Index Product

In the preliminary validation process, we inverted the refractive index product based on GPS L1 and BDS B1 single-frequency RO data, and the precision compared to the ERA5 reanalysis is satisfactory. Furthermore, the precision of the single/dual-frequency occultation process for refractive index products is within the same order of magnitude, indicating the correctness of the single-frequency occultation process in Section 2. In this section, we process the actual FY3E/GNOS Galileo E1 single-frequency occultation observation data.

The reference standard for the refractive index product of a single-frequency occultation process is ERA5 reanalysis. ERA5 reanalysis is a reliable compilation of extensive observed data from satellites, weather stations, buoys, and ships, as well as predictive data from climate models. It provides comprehensive meteorological data covering global and all weather conditions, including temperature, humidity, precipitation, wind speed, air pressure, cloud cover, and surface radiation. These data can be downloaded for free from the website [29]. ERA5 reanalysis does not directly provide the refractive index. Instead, Equation (12) is used to convert specific humidity and air pressure from the analysis data into water vapor pressure. Then, employing the aforementioned Equation (10), the water vapor pressure and atmospheric temperature are converted into the refractive index.

$$P_W = \frac{P \cdot q}{\varepsilon + (1 - \varepsilon) \cdot q} \tag{12}$$

where q represents the specific wetness, g/kg; $\varepsilon = \frac{R_d}{R_v}$, R_d and R_v represent the dry air and wet air gas constants, respectively, $\varepsilon \approx 0.622$. The remaining parameters have the same meaning as the parameters in Section 2.

The refractive index profiles obtained from Galileo single-frequency occultation data are compared with those calculated from ERA5 reanalysis. The average deviation index and RMS error index are calculated to analyze the level of deviation between the two. The experiment statistically analyzed the FY3E actual measured Galileo E1 single-frequency RO data on 3 January and 10 January 2022. The precision of the inverted refractive index is shown in Figure 10. The solid line reflects the average deviation percentage between processed by Galileo single-frequency occultation and calculated using ERA5 reanalysis. The dashed line represents the distribution of the RMS deviation between the two, with an auxiliary line indicating the 2% level. The two subfigures show similar trends in their variations.

From the solid line in the figure, the average deviation of the refractive index is less than 1% and is distributed near zero between heights of 5 km and 40 km. The consistency between the Galileo E1 single-frequency RO and the ERA5 reanalysis is very high, with the RMS error below 2%.

At lower altitudes near the Earth's surface, the average deviation index of the refractive index is relatively larger. This deviation may be due to imperfect attenuation of noise during the measurement caused by reconstructing the second frequency, even with the regularization method of minimizing the second-order derivative [30]. Furthermore, inverting the refractive index assumes atmospheric symmetry and utilizes the Abel integral transform of the bending angle. The Abel transform suppresses high-frequency noise to some extent. However, at lower altitudes of the atmosphere, there can be interference from ground reflections and the influence of turbulence, laminar flow, and inhomogeneities in the atmospheric layer. This leads to significant errors in the refractive index calculated using the Abel transform. When calculating the bending angle, errors are integrated and compounded, resulting in the final deviation.

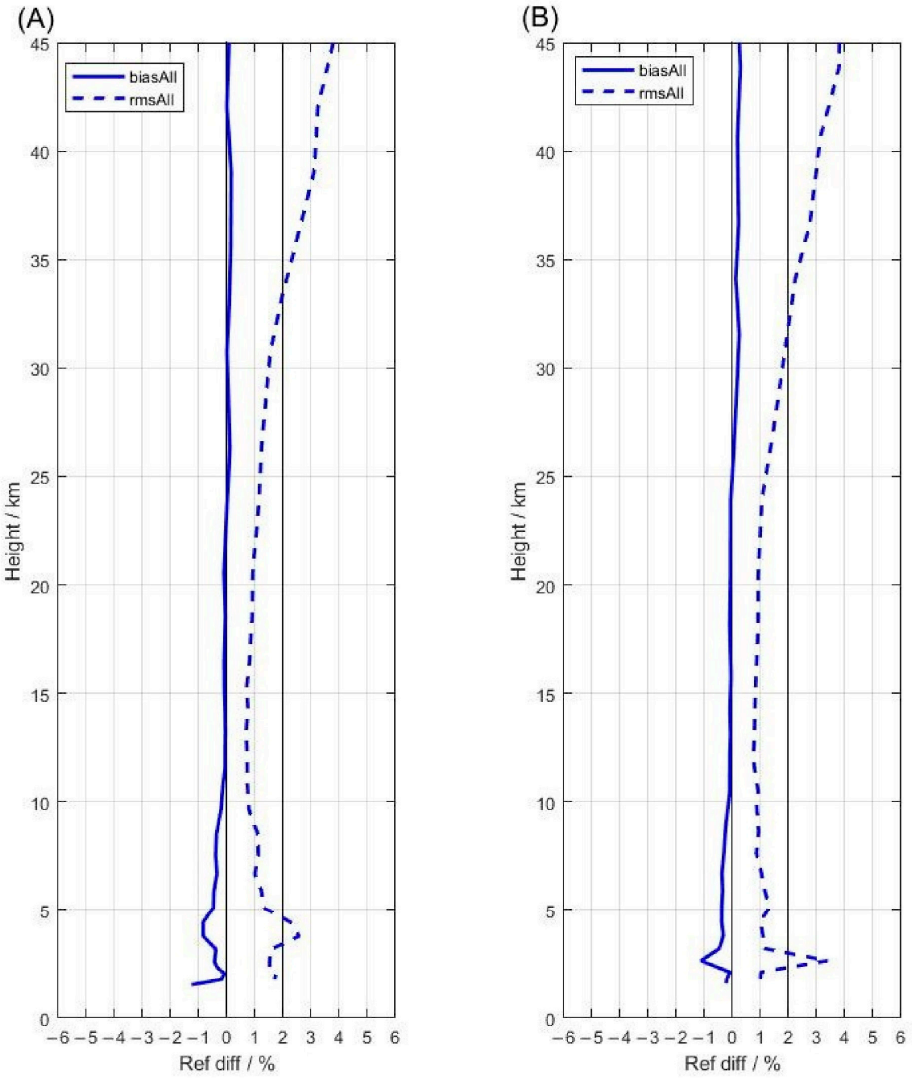

Figure 10. Refractive index product precision between Galileo E1 single-frequency RO and ERA5 reanalysis; (**A**) represents 3 January 2022 and (**B**) represents 10 January 2022.

At altitudes above 30 km, the overall RMS is less than 4%, but the deviation of the refractive index increases. The sources of error could be attributed to the following three reasons:

1. When reconstructing the second frequency carrier phase, pseudorange measurement noise is introduced. Additionally, even after smoothing the relTEC, there can still be residual noise from the ionosphere.
2. Errors in the prior climatological model near the transition layer have a certain impact on the precision of refractive index inversion in the upper atmosphere [31].
3. Because the actual background refractive index is smaller above 30 km, this leads to larger relative errors in the calculations.

We also statistics the lowest penetration height rate at which the occultation profile penetrated vertically through the atmosphere from 10 to 12 January 2022 in the Figure 11. Among the 984 Galileo RO events that can be inverted by refractive index products, nearly 49% of the lowest penetration heights are between 5 and 8 km deep, and the frequency of RO events below 5 km and above 8 km is 29% and 22%, respectively. Due to resource limitations, Galileo RO does not employ an open loop tracking mode in the lower atmospheric layers. Instead, only occultation events with closed loop tracking in the lower atmosphere are used. This leads to a number reduction in the effective occultation observations below 5 km.

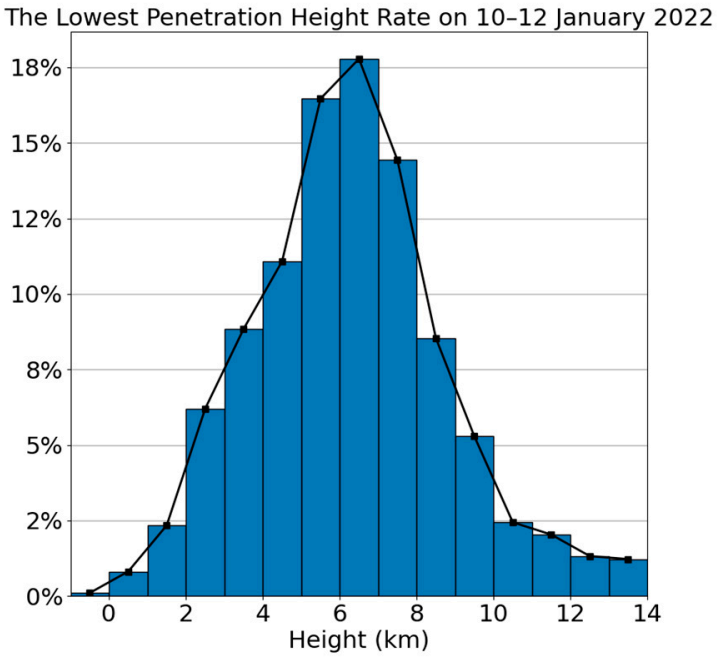

Figure 11. The lowest penetration height rate on 10–12 January 2022.

3.3. Precision Analysis of Dry Temperature Product

To further understand the impact of different geographical locations on the Galileo single-frequency occultation temperature product, Figure 12 presents the dry temperature precision profiles for various latitudes from 1 to 14 January 2022. The solid line represents the average deviation between the temperature inverted from Galileo single-frequency RO and ERA5 reanalysis. The dashed line represents the RMS error of the deviations. Subplots (A–C) correspond to statistical comparisons of low latitude (up to 30°N/S), mid-latitude (between 30° and 60°), and high latitude (above 60°) regions, respectively.

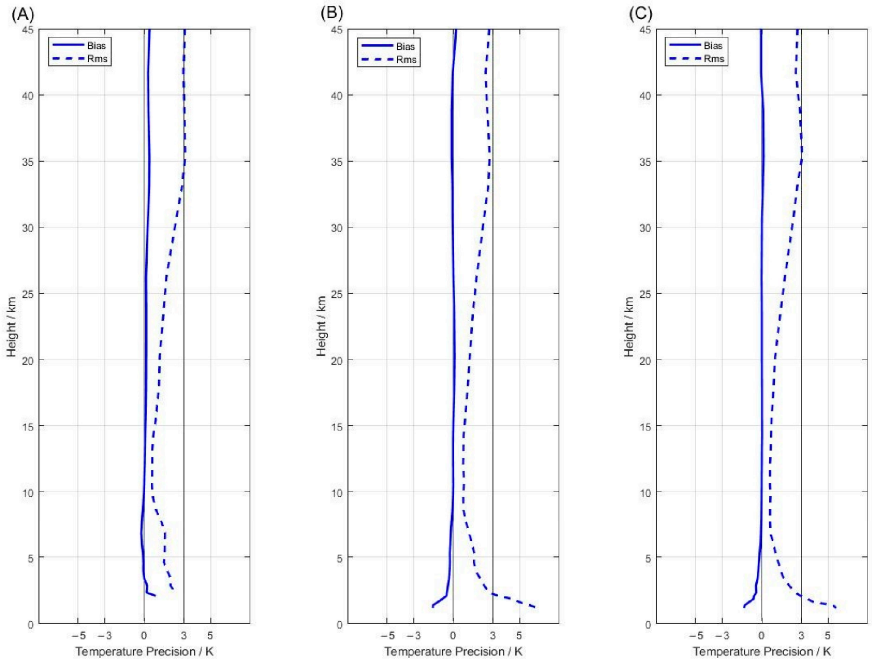

Figure 12. Dry temperature product precision between Galileo E1 single-frequency RO and ERA5 reanalysis accuracy profiles from 1 to 14 January 2022, obtained from regions of low latitude (**A**), mid latitude (**B**), and high latitude (**C**).

Regardless of the low-, mid-, or high-latitude Galileo single-frequency occultation temperature product, the precision characteristics are quite similar. In terms of average deviation, the temperature products show almost no bias compared to the ERA5 reanalysis. Analyzing the RMS, the average temperature differences within the 5–35 km altitude range have an RMS below 3 K. Above 30 km altitude, the RMS rapidly increases and remains at approximately 3 K beyond 35 km. The temperature precision profiles exhibit good consistency and reliability within the 5–30 km range.

From Figure 12A, at altitudes of 5 km and below, there are fewer effective data available. This is because, compared to high latitudes, lower latitudes have higher atmospheric humidity, and the higher humidity environment poses significant challenges for signal closure tracking [32,33]. It is worth noting due to resource constraints, GNOS receives the single-frequency Galileo RO signals in closed-loop mode, the tracking height is higher than that of the middle and high latitudes.

4. Summary

The Galileo occultation signal reception of the GNOS payload designed for the Fengyun3 series E/F/G/H satellites is based on the E1 single frequency. In this study, the actual Galileo single-frequency RO data obtained from the FY3E/GNOS receiver are used for the single-frequency occultation process. In terms of the number of occultation observations, the Galileo atmospheric occultation events received by FY3E/GNOS are distributed globally, similar to BDS and GPS occultation observations. The distribution is uniform, and the quantity is stable, which effectively improves the output of FY3E/GNOS occultation products and provides more data sources for global numerical weather prediction.

This study evaluates the precision of the products inverted from Galileo single-frequency RO data. The refractive index product and dry temperature product show good precision in the altitude range of 5–30 km. However, at lower altitudes, there are influences from ground reflections and the presence of turbulence, laminar flow, and inhomogeneities, which result in slightly larger biases in the refractive index and dry temperature average deviation. In the upper atmosphere, the inversion products are affected by high-frequency ionospheric and residual pseudorange noise, leading to increased errors.

In summary, the actual Galileo E1 single-frequency occultation data received by GNOS are accurate. The inversion products of single-frequency Galileo occultation serve as a valuable supplement to the FY3 occultation products, thereby enhancing the quantity of global occultation products.

5. Discussion

The GNSS RO remote sensing payload GNOS carried on FY3E for measuring atmospheric occultation data has the unique feature of receiving occultation signals from the GPS, BDS, and Galileo constellations simultaneously. However, the Galileo occultation signals received by FY3E/GNOS are single frequency. This study demonstrates the precise refractive index product and dry temperature product, indicating the correctness of Galileo single-frequency GNSS RO data. Therefore, it can contribute to increasing the number of global occultation events for numerical weather prediction.

The precision of single-frequency occultation process products above 30 km is significantly affected by factors such as high-frequency ionospheric and pseudorange noise residuals. However, the single-frequency occultation process products in the range of 5–30 km possess a considerable level of reliability. In terms of numerical assimilation and related applications, it is recommended to decrease the weighting of single-frequency process products below 5 km and above 30 km. The single-frequency occultation process employed in this study is derived from the Ørsted satellite and has been successfully validated in the FY3E GPS and BDS single-frequency occultation processes. It has also been applied to Galileo's single-frequency occultation process. It is believed that this method has the potential to be applied to single-frequency occultation processes in other satellite occultation missions to increase the number of available occultation events.

Not only for the single-frequency occultation process but also for the L2P band of the GPS dual-frequency occultation process, which exhibits poor tracking near the bottom of the atmosphere, the method of second frequency reconstruction introduced in this paper can be considered to eliminate ionospheric errors. This means that a single-frequency occultation process can to some extent enhance the number of occultation data sources for global numerical weather prediction, thereby improving its precision. If there is more support from GNSS RO inversion data for research on numerical weather prediction and global climate change, it will greatly enhance the application capabilities of meteorological services, regardless of whether these GNSS RO inversion products come from dual-frequency or single-frequency occultation data.

Author Contributions: Conceptualization, X.M., Q.D., W.B. and Y.S.; methodology, X.M., H.T., Y.S., Q.D., B.W. and X.W.; software, X.M., H.T., P.H., G.T. and B.W.; data curation, X.M.; formal analysis. M.Y.; writing—original draft preparation, M.Y. and H.T.; writing—review and editing, X.M. and M.Y.; project administration, Y.S., Q.D. and W.B.; funding acquisition: Y.S., Q.D. and W.B.; All authors have read and agreed to the published version of the manuscript.

Funding: This work is supported by the National Natural Science Foundation of China (42074042 and 41775034, 42104032) and in part by the Youth Cross Team Scientific Research Project of the Chinese Academy of Sciences (JCTD-2021-10).

Data Availability Statement: The ECMWF ERA5 reanalysis is available at: https://cds.climate.copernicus.eu/cdsapp#!/dataset/reanalysis-era5-pressure-levels?tab=form (accessed on 21 January 2022). The observations are available at: https://www.scidb.cn/anonymous/bjJFWlJy (accessed on 28 July 2023).

Acknowledgments: The authors would like to acknowledge National Satellite Meteorological Center of the China Meteorological Administration for providing the FY3E/GNOS occultation observation data. We also extend our thanks to the GFZ Analysis Center of the International GNSS Service for providing the precise ephemeris products of the GNSS Beidou System. Additionally, we appreciate the European Centre for Medium-Range Weather Forecasts for providing the ERA5 reanalysis field data products.

Conflicts of Interest: The authors declare no conflict of interest.

References

1. Kliore, A.; Levy, G.S.; Cain, D.L.; Eshleman, V.R.; Fjeldbo, G.; Drake, F.D. Mariner 4 Measurements Near Mars—Initial Results—Occultation Experiment—Results of 1st Direct Measurement of Mars Atmosphere and Ionosphere. *Science* **1965**, *149*, 1243–1248. [CrossRef]
2. Fischbach, F.F. A Satellite Method for Pressure and Temperature below 24 km. *Bull. Am. Meteorol. Soc.* **1965**, *46*, 528–532. [CrossRef]
3. Yunck, T.P.; Melbourne, W.G.; Thornton, C.L. GPS-based satellite tracking system for precise positioning. *IEEE Trans. Geosci. Remote Sens.* **1985**, *23*, 450–457. [CrossRef]
4. Sun, Y.Q.; Wang, B.W.; Meng, X.G.; Tang, X.C.; Yan, F.; Zhang, X.G.; Bai, W.H.; Du, Q.F.; Wang, X.Y.; Cai, Y.R.; et al. Analysis of Orbital Atmospheric Density from QQ-Satellite Precision Orbits Based on GNSS Observations. *Remote Sens.* **2022**, *14*, 3873. [CrossRef]
5. Anthes, R.A. Exploring Earth's atmosphere with radio occultation: Contributions to weather, climate and space weather. *Atmos. Meas. Tech.* **2011**, *4*, 1077–1103. [CrossRef]
6. Boonyuen, P.; Wu, F.L.; Phunthirawuth, P.; Zhao, Y. Impact of GPS RO and Radiance Data Assimilation on Numerical Weather Prediction. In Proceedings of the 36th IEEE International Geoscience and Remote Sensing Symposium (IGARSS), Beijing, China, 10–15 July 2016; pp. 2185–2188.
7. Ho, S.P.; Anthes, R.A.; Ao, C.O.; Healy, S.; Horanyi, A.; Hunt, D.; Mannucci, A.J.; Pedatella, N.; Randel, W.J.; Simmons, A.; et al. The COSMIC/FORMOSAT-3 Radio Occultation Mission after 12 Years Accomplishments, Remaining Challenges, and Potential Impacts of COSMIC-2. *Bull. Am. Meteorol. Soc.* **2020**, *101*, E1107–E1136. [CrossRef]
8. Bi, Y.M.; Yang, Z.D.; Zhang, P.; Sun, Y.Q.; Bai, W.H.; Du, Q.F.; Yang, G.L.; Chen, J.; Liao, M. An introduction to China FY3 radio occultation mission and its measurement simulation. *Adv. Space Res.* **2012**, *49*, 1191–1197. [CrossRef]
9. Yang, G.L.; Bai, W.H.; Wang, J.S.; Hu, X.Q.; Zhang, P.; Sun, Y.Q.; Xu, N.; Zhai, X.C.; Xiao, X.J.; Xia, J.M.; et al. FY3E GNOS II GNSS Reflectometry: Mission Review and First Results. *Remote Sens.* **2022**, *14*, 988. [CrossRef]
10. Sun, Y.Q.; Wang, X.Y.; Du, Q.F.; Bai, W.H.; Xia, J.M.; Cai, Y.R.; Wang, D.W.; Wu, C.J.; Meng, X.G.; Liu, C.L.; et al. The Status and Progress of Fengyun-3e GNOS II Mission for GNSS Remote Sensing. In Proceedings of the IEEE International Geoscience and Remote Sensing Symposium (IGARSS), Yokohama, Japan, 28 July–2 August 2019; pp. 5181–5184.

11. China Satellite Navigation Office BeiDou/Global Navigation Satellite System (GNSS) Radio Occultation Sounder Data Independent Exchange Format. 2022. Available online: https://www.beidou.gov.cn/ (accessed on 30 December 2022).
12. Montenbruck, O. Kinematic GPS positioning of LEO satellites using ionosphere-free single frequency measurements. *Aerosp. Sci. Technol.* **2003**, *7*, 396–405. [CrossRef]
13. Larsen, G.B.; Syndergaard, S.; Hoeg, P.; Sorensen, M.B. Single frequency processing of Orsted GPS radio occultation measurements. *Gps Solut.* **2005**, *9*, 144–155. [CrossRef]
14. Bai, W.H.; Liu, C.L.; Meng, X.G.; Sun, Y.Q.; Kirchengast, G.; Du, Q.F.; Wang, X.Y.; Yang, G.L.; Liao, M.; Yang, Z.D.; et al. Evaluation of atmospheric profiles derived from single- and zero-difference excess phase processing of BeiDou radio occultation data from the FY-3C GNOS mission. *Atmos. Meas. Tech.* **2018**, *11*, 819–833. [CrossRef]
15. Tian, H.R.; Meng, X.G.; Du, Q.F.; Sun, Y.Q.; Bai, W.H.; Wang, X.Y.; Yang, M.; Tan, G.Y.; Hu, P. Verification and Accuracy Analysis of Single-Frequency Processing Based on GPS Radio Occultation. *J. Geod. Geodyn.* **2023**, *43*, 750–754. [CrossRef]
16. Li, R.M.; Du, Q.F.; Yang, M.; Tian, H.R.; Sun, Y.Q.; Meng, X.G.; Bai, W.H.; Wang, X.Y.; Tan, G.Y.; Hu, P. Verification and Accuracy Analysis of Single-Frequency Occultation Processing Based on the BeiDou Navigation System. *Atmosphere* **2023**, *14*, 742. [CrossRef]
17. Liao, M.; Healy, S.; Zhang, P. Processing and quality control of FY-3C GNOS data used in numerical weather prediction applications. *Atmos. Meas. Tech.* **2019**, *12*, 2679–2692. [CrossRef]
18. Wang, S.Z.; Zhu, G.W.; Bai, W.H.; Liu, C.L.; Sun, Y.Q.; Du, Q.F.; Wang, X.Y.; Meng, X.G.; Yang, G.L.; Yang, Z.D.; et al. For the first time fengyun3 C satellite-global navigation satellite system occultation sounder achieved spaceborne Bei Dou system radio occultation. *Acta Phys. Sin.* **2015**, *64*, 089301. [CrossRef]
19. Yang, M.; Meng, X.G.; Sun, Y.Q.; Du, Q.F.; Bai, W.H.; Wang, X.Y.; Yang, G.L.; Liao, M.; Hu, P.; Tan, G.Y. Preliminary Results of GPS-Based Precision Orbit Determination of FY-3E Satellite GNOS Dual-Antenna. In Proceedings of the 13th China Satellite Navigation Conference (CSNC)—Digital Economy and Intelligent Navigation, Beijing, China, 25–27 May 2022; pp. 209–219.
20. Juarez, M.D.; Hajj, G.A.; Kursinski, E.R.; Kuang, D.; Mannucci, A.J.; Romans, L.J. Single frequency processing of atmospheric radio occultations. *Int. J. Remote Sens.* **2004**, *25*, 3731–3744. [CrossRef]
21. Withers, P.; Moore, L.; Cahoy, K.; Beerer, I. How to process radio occultation data: 1. From time series of frequency residuals to vertical profiles of atmospheric and ionospheric properties. *Planet. Space Sci.* **2014**, *101*, 77–88. [CrossRef]
22. Withers, P.; Moore, L. How to Process Radio Occultation Data: 2. From Time Series of Two-Way, Single-Frequency Frequency Residuals to Vertical Profiles of Ionospheric Properties. *Radio Sci.* **2020**, *55*, e2019RS007046. [CrossRef]
23. Beyerle, G.; Schmidt, T.; Michalak, G.; Heise, S.; Wickert, J.; Reigber, C. GPS radio occultation with GRACE: Atmospheric profiling utilizing the zero difference technique. *Geophys. Res. Lett.* **2005**, *32*. [CrossRef]
24. Montenbruck, O.; Hauschild, A.; Andres, Y.; von Engeln, A.; Marquardt, C. (Near-)real-time orbit determination for GNSS radio occultation processing. *GPS Solut.* **2013**, *17*, 199–209. [CrossRef]
25. Pavelyev, A.G.; Liou, Y.A.; Wickert, J.; Pavelyev, A.A.; Electromagnetics, A. Identification and Localization of Layers in the Atmosphere and Ionosphere Based on Observing Variations in the Phase and Amplitude of Radio Waves along the Satellite-to-satellite Path. In Proceedings of the Progress in Electromagnetics Research Symposium (PIERS 2009 Moscow), Moscow, Russia, 12–21 August 2009; pp. 213–218.
26. Scherllin-Pirscher, B.; Syndergaard, S.; Foelsche, U.; Lauritsen, K.B. Generation of a bending angle radio occultation climatology (BAROCLIM) and its use in radio occultation retrievals. *Atmos. Meas. Tech.* **2015**, *8*, 109–124. [CrossRef]
27. Lauritsen, K.B.; Syndergaard, S.; Gleisner, H.; Gorbunov, M.E.; Rubek, F.; Sorensen, M.B.; Wilhelmsen, H. Processing and validation of refractivity from GRAS radio occultation data. *Atmos. Meas. Tech.* **2011**, *4*, 2065–2071. [CrossRef]
28. Gorbunov, M.E.; Shmakov, A.V. Statistically average atmospheric bending angle model based on COSMIC experimental data. *Izv. Atmos. Ocean. Phys.* **2016**, *52*, 622–628. [CrossRef]
29. Li, J.Y.; Zhang, B.; Yao, Y.B.; Liu, L.L.; Sun, Z.Y.; Yan, X. A Refined Regional Model for Estimating Pressure, Temperature, and Water Vapor Pressure for Geodetic Applications in China. *Remote Sens.* **2020**, *12*, 1713. [CrossRef]
30. Anthes, R.A.; Bernhardt, P.A.; Chen, Y.; Cucurull, L.; Dymond, K.F.; Ector, D.; Healy, S.B.; Ho, S.P.; Hunt, D.C.; Kuo, Y.H.; et al. The COSMIC/FORMOSAT-3 Mission: Early Results. *Bull. Am. Meteorol. Soc.* **2008**, *89*, 313–333. [CrossRef]
31. Mousa, A.E.K.; Tsuda, T. Analysis of down looking GPS occultation simulated data using least squares and abel inversions. In Proceedings of the NATO Advanced Research Workshop on Regional Climate Variability and its Impacts in the Mediterranean Area, Marrakech, Morocco, 1 September 2006; p. 279.
32. Xu, X.H.; Luo, J.; Shi, C.A. Comparison of COSMIC Radio Occultation Refractivity Profiles with Radiosonde Measurements. *Adv. Atmos. Sci.* **2009**, *26*, 1137–1145. [CrossRef]
33. Vergados, P.; Mannucci, A.J.; Ao, C.O.; Jiang, J.H.; Su, H. On the comparisons of tropical relative humidity in the lower and middle troposphere among COSMIC radio occultations and MERRA and ECMWF data sets. *Atmos. Meas. Tech.* **2015**, *8*, 1789–1797. [CrossRef]